JOURNAL OF THE AMERICAN CHEMICAL SOCIETY

# Square-Planar Tetranuclear Cluster-Based High-Symmetry Coordination Metal–Organic Polymers for Efficient Electrochemical Nitrate Reduction to Ammonia

Miao Wang,[⊥] Ya-Ru Meng,[⊥] Wenjie Xu,[⊥] Tianyu Shen,[⊥] Yunhao Wang, Qianchuan Yu, Chongjing Liu, Yuming Gu, Zuoxiu Tie, Zhanxi Fan, Jing-Lin Zuo,* Jian Su,* and Zhong Jin*

**Cite This:** *J. Am. Chem. Soc.* 2025, 147, 18327−18337

Read Online

ACCESS | Metrics & More | Article Recommendations | Supporting Information

**ABSTRACT:** Metal–organic polymers (MOPs) are gaining booming attention as atomically precise single-site catalysts for electrochemical nitrate-to-ammonia conversion owing to their regular structures and tunable functionalities. However, a molecular-level understanding is still lacking for the design of more efficient MOP electrocatalysts. Here, we report the construction of high-symmetry coordination MOPs (**Mn-TATB**, **Fe-TATB**, and **Co-TATB**), utilizing square-planar tetranuclear building units $[M_4(\mu_4\text{-}O)(CO_2)_8]$ (M = Mn, Fe, or Co) bridged by 2,4,6-tris(4-carboxyphenyl)-1,3,5-triazine ($H_3TATB$) ligands. These MOPs possess distinct coordination motifs with well-defined porosity, high-density catalytic sites, accessible mass transfer channels, and nanoconfined chemical environments. Benefited from the unique metal–organic coordination framework, **Co-TATB** demonstrated a remarkable ammonia production Faradaic efficiency ($FE_{NH3}$) of ~98% across a wide potential range (−0.7 to −1.0 V (vs RHE)) in the electrocatalytic nitrate reduction reaction (NITRR) and maintained stable performance over a long duration when tested in a flow cell at an industrially relevant current density of ~332.1 mA $cm^{-2}$. Furthermore, in situ spectroscopic analyses, combined with theoretical calculations, elucidate the intrinsic reaction pathway of the **Co-TATB** model during the NITRR process. These findings offer insightful perspectives on the strategic design of electrocatalysts with symmetrical configurations for the purification of nitrate-containing wastewater and the green synthesis of ammonia.

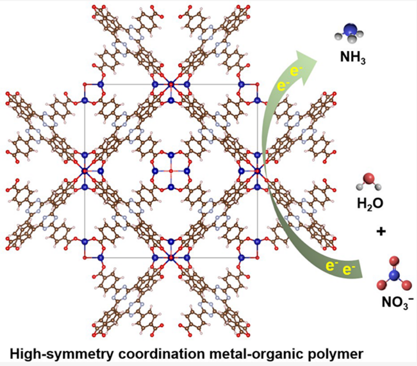

## ■ INTRODUCTION

The nitrogen cycle is essential for maintaining the ecological balance of natural ecosystems and human society.[1,2] Nitrogen, a vital component for all living organisms, exists in various forms across the atmosphere, water, soil, and biological systems, interconverting through the nitrogen cycle.[3] Over a century ago, the Haber–Bosch process facilitated the artificial conversion of atmospheric nitrogen ($N_2$) to ammonia ($NH_3$), making ammonia fertilizers widely accessible. However, this industrial method is energy-intensive and has a significant carbon footprint.[4] In contrast, direct synthesis of $NH_3$ through electrochemical reduction of $N_2$ under mild conditions presents a promising approach, albeit with challenges due to the chemical inertness of $N_2$, which results in slow reaction rates.[5−10] Alternatively, synthesizing $NH_3$ via the electrochemical nitrate reduction reaction (NITRR) is more kinetically favorable and has garnered increasing interest recently.[11−15] Interestingly, nitrate sources can be produced from atmospheric $N_2$ by using plasma treatments, allowing for the indirect fixation of nitrogen. This reaction can also be driven by renewable energy sources, such as solar, hydro, and wind power, potentially leading to emissions-free processes. Furthermore, nitrates ($NO_3^-$) are recognized as significant environmental pollutants, and their reduction can produce harmful nitrosamines linked to serious health risks, including cancer.[16] Thus, electrocatalytic NITRR not only provides a method for producing value-added $NH_3$ but also serves as a feasible strategy for purifying the nitrates from overfertilized water bodies, addressing both eutrophication and the pressing global challenge of water security.

In essence, the NITRR involves the participation of eight electrons and nine protons, represented by the equation: $NO_3^- + 6H_2O + 8e^- \rightarrow NH_3 + 9OH^-$. This process requires a substantial amount of active hydrogen (H*). This involves facilitating efficient water dissociation to generate H* through the active sites and ensuring that the spacing between these sites minimizes H* binding into $H_2$. If the availability of H* at the active sites is limited, side reactions may occur, leading to

**Received:** April 19, 2025
**Revised:** May 5, 2025
**Accepted:** May 7, 2025
**Published:** May 14, 2025

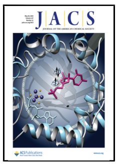

https://doi.org/10.1021/jacs.5c06650
*J. Am. Chem. Soc.* 2025, 147, 18327−18337

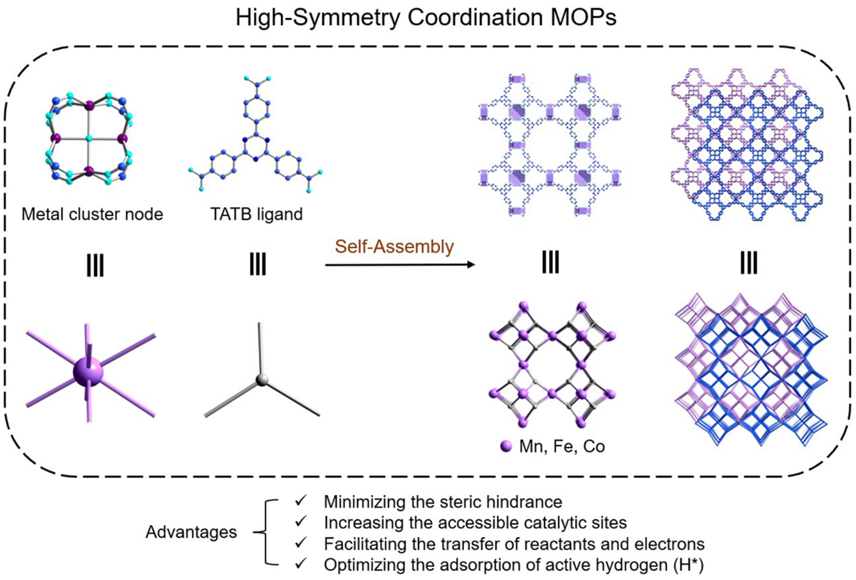

**Figure 1.** Structural assembly of square-planar tetranuclear cluster-based high-symmetry coordination MOPs. Schematic representation of the structural assembly process and crystal structures of the high-symmetry coordination MOPs (M = Mn, Fe, or Co). The diagram illustrates the connection of tetranuclear $[M_4(\mu_4\text{-}O)(CO_2)_8]$ building units to organic TATB ligands.

decreased ammonia production, Faradaic efficiency ($FE_{NH3}$), and ammonia yield. Especially, the conversion of reactive H* into $H_2$ can significantly impact the distribution of products since the hydrogen evolution reaction (HER) presents a strong competitive side reaction that undermines ammonia production performance.[17] Recently, atomically precise metal–organic polymers (MOPs) have emerged as promising candidates for enhancing NITRR activity.[18–25] Their unique structural attributes, featuring well-defined metal–organic coordination networks with multitiered channels, consistent porosity, and adjustable electron/ion transport properties, derive from miscellaneous ligand design, rendering them particularly attractive. However, there remains a gap in the molecular-level understanding necessary for the rational design of highly active and stable MOPs.

Herein, we present a molecular engineering approach to develop a series of highly symmetric coordinated MOPs (**Mn-TATB**, **Fe-TATB**, and **Co-TATB**) via the self-assembly of square-planar tetranuclear $[M_4(\mu_4\text{-}O)(CO_2)_8]$ (where M = Mn, Fe, or Co) building blocks paired with 2,4,6-tris(4-carboxyphenyl)-1,3,5-triazine ($H_3$TATB) ligands (as depicted in Figure 1). The square-planar metal coordination structures have notable advantages in further increasing the number of active sites, minimizing steric hindrance, and facilitating the transfer of reactants and electrons. Especially, the planar coordination structures comprising distinct metal or cluster centers alongside functional organic linkers/groups inherently provide ample catalytic sites and favor the adsorption of active hydrogen (H*). In contrast, the polyhedral structures of metal atoms, such as tetrahedral coordination, make the adsorption of H* more difficult, resulting in a spatial configuration that is less favorable for further catalytic hydrogenation reactions of nitrate species. Electrocatalytic tests demonstrate their outstanding performance in selective NITRR, achieving a remarkable $FE_{NH3}$ of approximately 98% for ammonia production on the **Co-TATB** electrode across a broad potential range of −0.7 to −1.0 V (vs RHE) under ambient conditions. When tested in a flow cell at an industrially relevant current density of ~332.1 mA $cm^{-2}$, the **Co-TATB** electrode maintained a stable performance over a long duration, showing no significant decline in $FE_{NH3}$. In situ spectroscopic analyses coupled with theoretical calculations reveal the reaction pathway of **Co-TATB** during the NITRR process. This study highlights the intrinsic structure–activity relationship of high-symmetry coordination MOPs in NITRR, offering valuable insights for the rational design of next-generation electrocatalysts toward clean energy conversion and sustainable development.

## ■ RESULTS AND DISCUSSION

**Morphological and Structural Characterizations.** Three isomorphic MOPs, denoted as **Mn-TATB**, **Fe-TATB**, and **Co-TATB**, with the formula $[M_4(\mu_4\text{-}O)(TATB)_{8/3}]$ (where M = Mn, Fe, Co), were synthesized via a solvothermal method (Figure 1). These high-symmetry coordination MOP crystals exhibit a regular cubic morphology, as shown in Figure 2a–c. All three MOPs crystallize in the *I*m3m space group within the cubic crystal system. Each metal atom is five-coordinate, forming bonds with four oxygen atoms from carboxylates and one oxygen atom from the $\mu_4$-O. In particular, the four metal atoms residing at a square-planar configuration are linked by a central oxygen atom ($\mu_4$-O) and coordinated with eight carboxylic acid groups from the TATB ligands, resulting in tetranuclear clusters as secondary building units (SBUs) $[[M_4(\mu_4\text{-}O)(CO_2)_8]]$ (Figures 2d and S1). The distinct characteristics of these MOPs are highlighted by the length differences in the M-$\mu_4$-O bonds: 2.194(3) Å for **Mn-TATB**, 2.313(3) Å for **Fe-TATB**, and 2.351(2) Å for **Co-TATB**, respectively (Figure S2). The sizes of the tetranuclear nodes are also distinct, measuring 3.103 Å × 3.103 Å for **Mn-TATB**, 3.270 Å × 3.270 Å for **Fe-TATB**, and 3.325 Å × 3.325 Å for **Co-TATB**, respectively. The assembly of the tetranuclear $[M_4(\mu_4\text{-}O)(CO_2)_8]$ clusters with TATB ligands creates two types of coordination cages. The first type is a truncated octahedral cage, formed by six metal clusters and eight organic ligands (Figure 2e), with a simplified structure depicted in Figure S3. The second type is a cuboctahedral cage, consisting of eight truncated octahedral cages situated at the vertices of

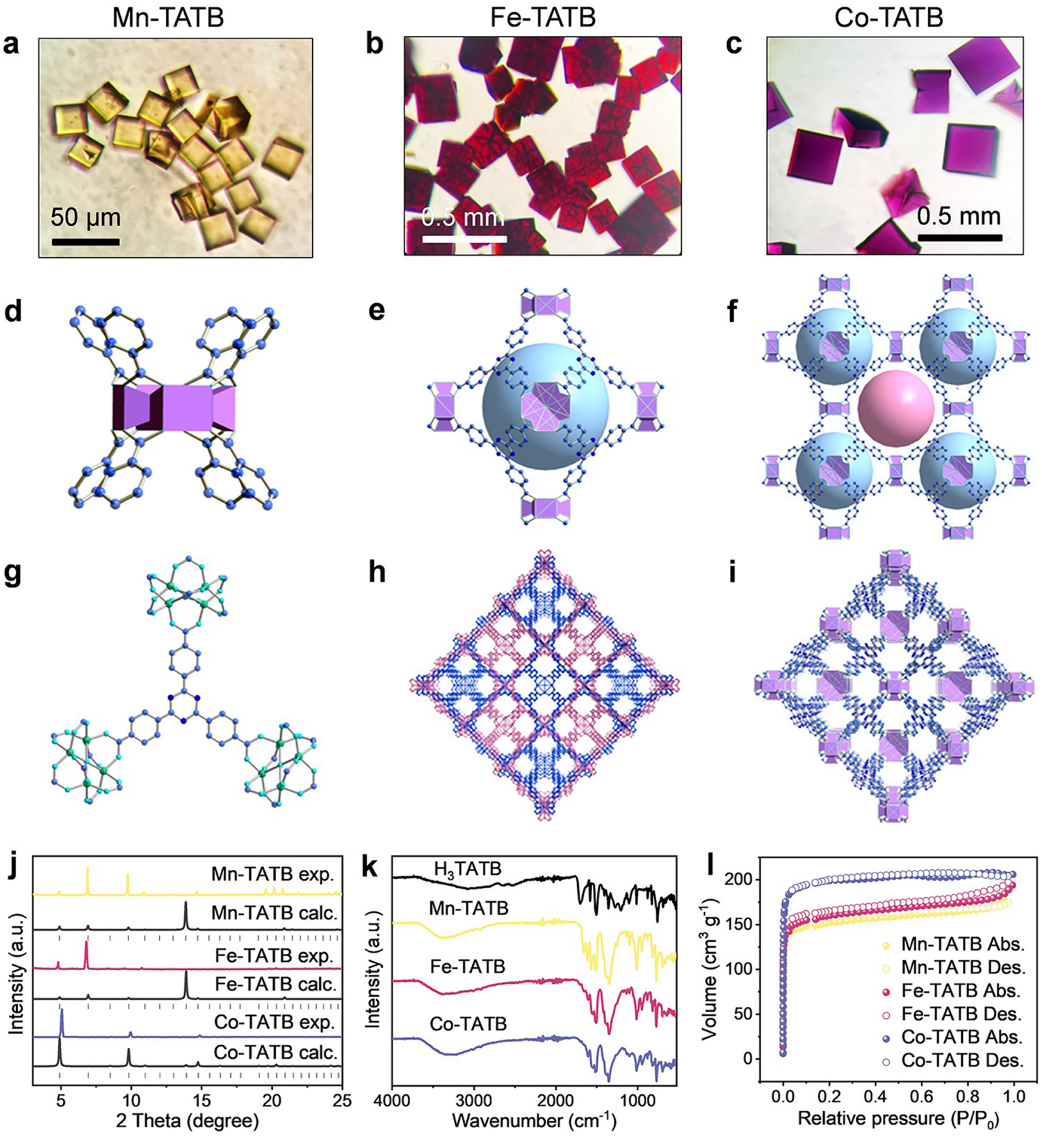

**Figure 2.** Morphological and structural characterizations of high-symmetry coordination MOPs. (a−c) Macroscopic crystal morphologies of (a) **Mn-TATB**, (b) **Fe-TATB**, and (c) **Co-TATB**, respectively. (d, e) Tetranuclear cluster nodes illustrating (d) the primary structural building block and (e) the octahedral cage structure of the MOPs. (f) Cubic cage architecture and the octahedral connectivity features within the MOPs. (g) Representation of the interaction between tetranuclear metal clusters and organic TATB ligands. (h) Visualization of the double interleaved network structure of the MOPs. (i) Overall three-dimensional framework of the MOPs. (j) Comparison of experimental and simulated PXRD patterns of as-synthesized MOP samples. (k) FTIR spectra of the MOPs. (l) $N_2$ adsorption−desorption isotherms of the MOPs.

the cube (Figure 2f). Each cuboctahedral cage shares faces with eight truncated octahedral cages, while each truncated octahedral cage connects to six cuboctahedral cages, establishing a long-range-ordered three-dimensional (8,3)-net. In the organic ligand portion, each TATB ligand features three carboxylic acid groups that engage in bidentate chelation with six metal atoms from three tetranuclear nodes (Figure 2g). Furthermore, two three-dimensional networks intertwine to produce a 2-fold interpenetrated framework, as displayed in Figure 2(h, i).

Powder X-ray diffraction (PXRD) analyses revealed that the as-prepared MOPs exhibit excellent crystallinity aligned with their proposed crystal structures, with no noticeable impurity phases detected, as displayed in Figures 2j and S4. Chemical stability tests conducted on **Mn-TATB**, **Fe-TATB**, and **Co-TATB** samples demonstrated that they remained stable in various organic solvents, including acetonitrile, chloroform, N,N-dimethylformamide (DMF), alcohols, and acetone (Figures S5−S7). Moreover, the MOP samples showed remarkable stability in aqueous solutions with a wide pH range (Figures S8−S10). Fourier-transform infrared (FTIR) spectroscopy results of the MOPs indicate that the characteristic C═O vibration peak at 1700 $cm^{-1}$ present in $H_3TATB$ disappears, signifying the successful coordination of the carboxylic acid group with the metal atoms (Figure 2k). Solid-state ultraviolet−visible-near-infrared (UV−vis−NIR) absorption spectroscopy results reveal that the characteristic peak of **Mn-TATB** in the range of 200−425 nm primarily originates from the UV absorption of organic ligands (200−400 nm). In contrast, **Fe-TATB** and **Co-TATB** absorb in the range of 300−650 and 400−700 nm, respectively, attributed to metal-to-ligand charge transfer (MLCT) or ligand-to-metal charge transfer (LMCT) (Figure S11). To assess the thermal stability, thermogravimetric analysis (TGA) was performed under a

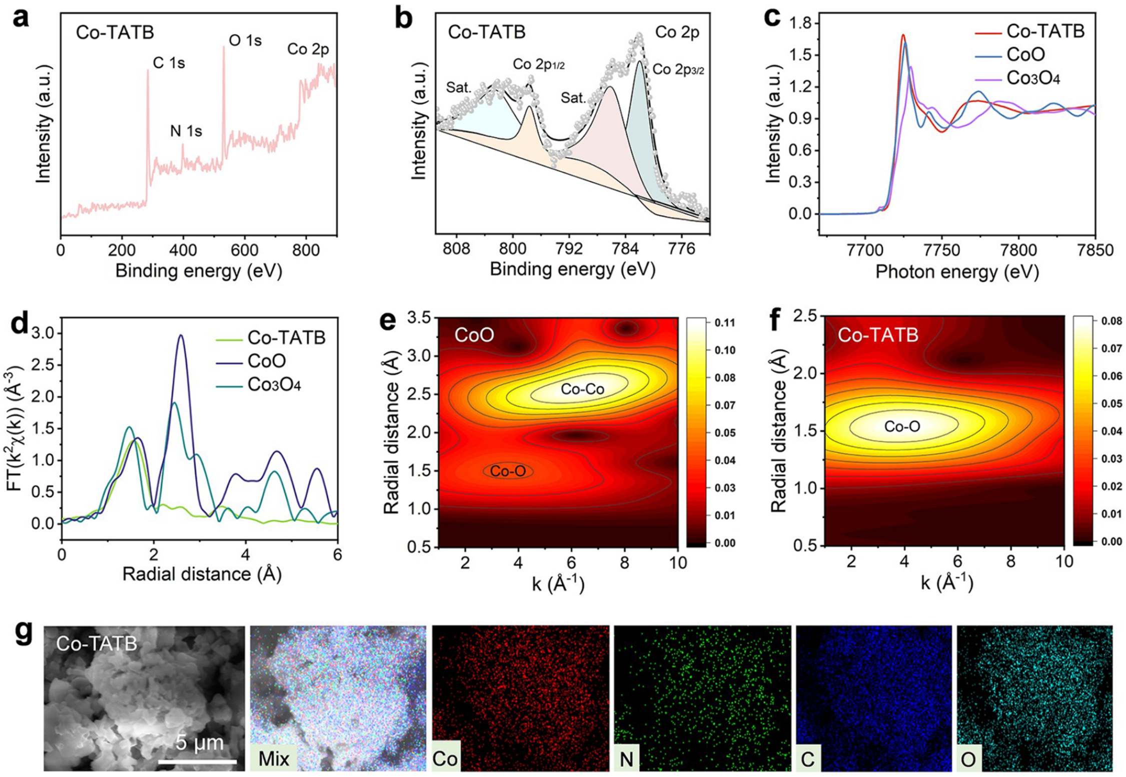

**Figure 3.** Structural and compositional characterizations of Co-TATB. (a) Survey XPS spectra of **Co-TATB**. (b) XPS spectra at the Co 2p level of **Co-TATB**. (c) Co K-edge XANES, and (d) EXAFS spectra of **Co-TATB** compared with reference samples. (e, f) Co K-edge wavelet transformation of (e) CoO and (f) **Co-TATB**, respectively. (g) SEM and elemental mapping images of **Co-TATB**.

nitrogen atmosphere (Figure S12). The TGA results of MOPs indicate initial weight loss below 100 °C, attributed to the loss of nine coordinated water molecules in the channels. A subsequent weight loss observed below 250 °C is due to solvent evaporation from the crystal surface and within the pores. **Fe-TATB** and **Co-TATB** maintain thermal stability up to 450 °C, while **Mn-TATB** withstands up to 500 °C. To evaluate the porosity, gas adsorption tests were conducted following solvent exchange with acetone and activation at 100 °C (Figure 2l). The nitrogen ($N_2$) adsorption isotherms at 77 K for all three MOPs exhibited typical type I adsorption characteristics. The adsorption capacities were measured at 140.0 $cm^3\ g^{-1}$ for **Mn-TATB**, 150.0 $cm^3\ g^{-1}$ for **Fe-TATB**, and 200.0 $cm^3\ g^{-1}$ for **Co-TATB**. Correspondingly, the Brunauer–Emmett–Teller (BET) surface areas were calculated to be 437, 468, and 594 $m^2\ g^{-1}$, respectively.

Survey X-ray photoelectron spectroscopy (XPS) of the as-synthesized **Co-TATB** sample confirms the presence of cobalt (Co), carbon (C), nitrogen (N), and oxygen (O) elements (Figure 3a). To analyze the chemical states of **Co-TATB**, high-resolution XPS spectrum at the Co 2p level was obtained, revealing characteristic peaks at approximately 781.9 and 797.6 eV, corresponding to the Co $2p_{3/2}$ and Co $2p_{1/2}$ bands of $Co^{2+}$ species, respectively (Figure 3b).[26,27] Additional satellite peaks are observed at ~786.2 and ~802.5 eV. Co K-edge X-ray absorption fine structure (XAFS) spectroscopy was utilized to investigate the local coordination environment and electronic structure of **Co-TATB**. The position of absorption edge suggests that the Co atoms in **Co-TATB** are divalent, closely resembling that of the CoO reference sample (Figure 3c).[28,29] The R-space plot reveals a main peak at 1.56 Å, attributed to Co–O coordination (Figure 3d). Wavelet transformation analysis further suggests a similarity in coordination features between **Co-TATB** and the CoO reference sample, as displayed in Figure 3e,f. Quantitative results from EXAFS fitting indicate that the coordination number for the metal Co atom in **Co-TATB** is approximately five, corresponding to four neighboring oxygen atoms from carboxylate groups and one additional central oxygen atom from the $\mu_4$-O unit (Table S1).

To further elucidate the local coordination structure of Co, we analyzed the pre-edge peaks in the XAFS spectra. Previous studies have shown that the pre-edge peak intensity increases as the coordination geometry transitions from octahedral to tetrahedral. After background subtraction, we examined the pre-edge feature of the sample (Figure S13). The pre-edge peak height of **Co-TATB** lies between those of CoO (fully octahedral coordination) and $Co_3O_4$ (partially tetrahedral coordination), suggesting an intermediate symmetry. The EXAFS results reveal a coordination number of 5 for Co, with one elongated bond length. This strongly suggests a $C_{4v}$ symmetric environment, where the Co center is coordinated by five oxygen atoms in a square pyramidal geometry. Morphological analysis via scanning electron microscopy (SEM) illustrates the morphology of **Co-TATB**, and elemental mapping confirms a homogeneous distribution of Co, N, C, and O elements within the sample (Figure 3g). Low-resolution and high-resolution transmission electron microscopy (TEM) images show the morphology of the **Co-TATB** sample that consists of its crystalline microstructure (Figures S14 and S15). The elemental distributions were further investigated by scanning TEM-energy dispersive X-ray (STEM-EDX) analysis. The results indicated that the elements were uniformly distributed in the **Co-TATB** sample, as displayed in Figure S15.

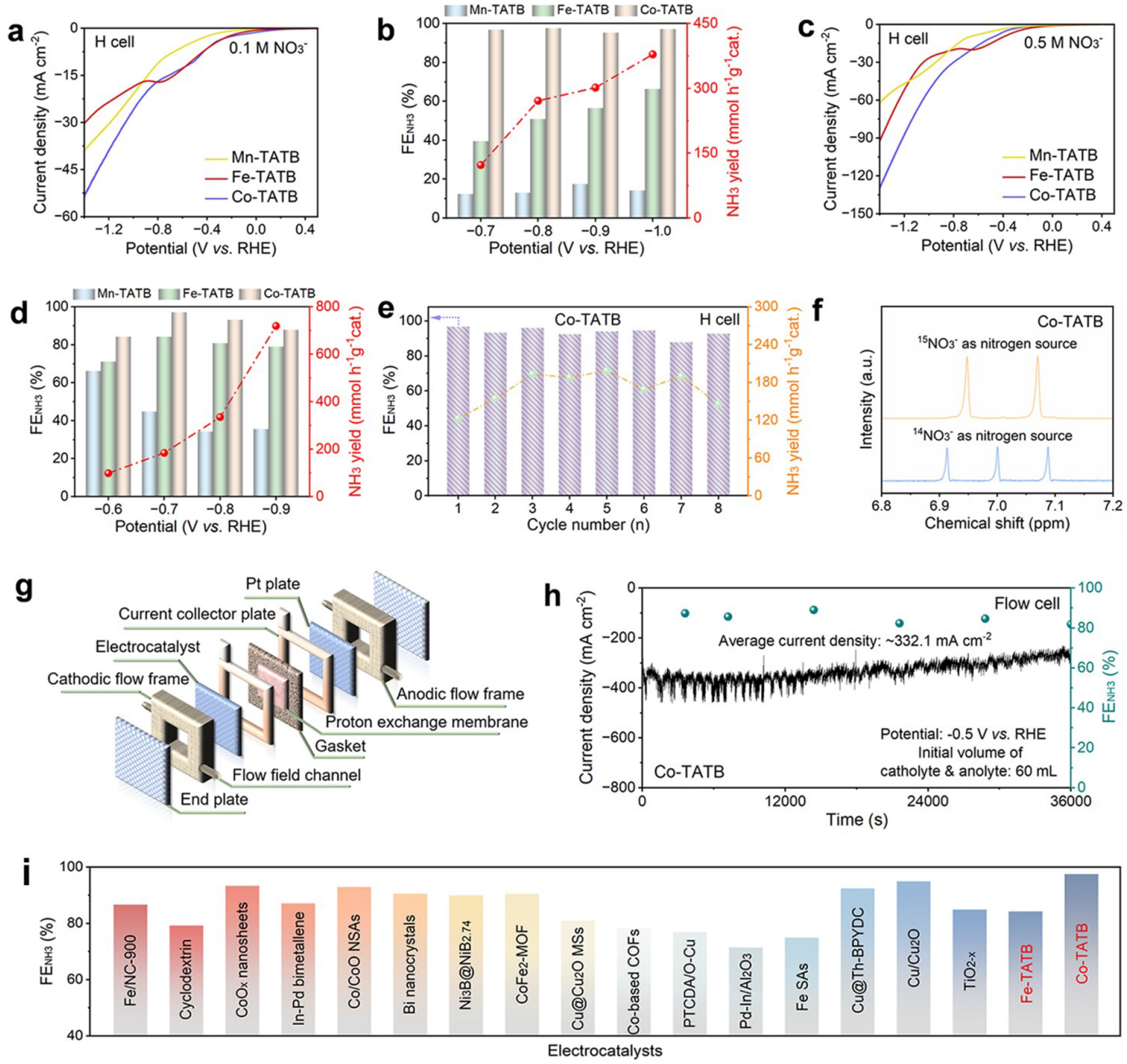

**Figure 4.** Electrocatalytic activities of high-symmetry coordination MOPs for the NITRR. (a) LSV curves and (b) $FE_{NH3}$ values (left Y axes) and corresponding $NH_3$ yield rates (right Y axes) of the MOPs tested in a 0.1 M $Na_2SO_4$–0.1 M $KNO_3$ mixed electrolyte at various applied potentials for the NITRR. (c) LSV curves and (d) $FE_{NH3}$ values (left Y axes) and corresponding $NH_3$ yield rates (right Y axes) of the MOPs tested in a 0.5 M $KNO_3$ electrolyte at various applied potentials for the NITRR. (e) Cycling tests of the **Co-TATB** electrocatalyst for the NITRR in a 0.1 M $Na_2SO_4$-0.1 M $KNO_3$ electrolyte at −0.7 V (vs RHE). (f) $^1H$ NMR spectra of the products after the NITRR test of **Co-TATB** using $K^{14}NO_3$ and $^{15}N$ isotope-labeled $Na^{15}NO_3$ as the feeding nitrogen sources, respectively. (g) Schematic illustration of the flow cell configuration. (h) Time-dependent working curve of the **Co-TATB** electrocatalyst measured in the flow cell under an industrially relevant current density with a 0.1 M $Na_2SO_4$–0.1 M $KNO_3$ electrolyte at −0.5 V (vs RHE). (i) Electrocatalytic performance comparison on the $FE_{NH3}$ values for **Fe-TATB** and **Co-TATB** with other representative electrocatalysts in previous literature.[30−45]

**Electrocatalytic NITRR Tests.** The electrocatalytic performances of three MOP electrodes for the NITRR were evaluated in an H-type cell under ambient conditions. The linear sweep voltammetry (LSV) curves of MOP electrodes tested with different nitrate electrolyte concentrations are shown in Figures 4a,c, S16, and S17, highlighting the distinct electrocatalytic activities of each electrode toward nitrate species. Time-resolved current density tests were conducted across a range of applied potentials over a 0.5-h operation period. As anticipated, the current density increased monotonically with more negative potentials. The ammonia production yields were quantified using UV−vis absorption spectra (Figures S18−S20). Overall, the electrocatalytic activity of the three MOP electrodes was ranked as follows: **Co-TATB** > **Fe-TATB** > **Mn-TATB**. Notably, **Co-TATB** exhibits an $FE_{NH3}$ of approximately 98% when tested in a mixed electrolyte of 0.1 M $Na_2SO_4$ and 0.1 M $KNO_3$ over a wide voltage range (−0.7 V to −1.0 V vs RHE), as shown in Figure 4b. Specifically, the $FE_{NH3}$ and ammonia yield rate of the **Co-TATB** electrode are 96.8% and 122.7 mmol $h^{-1}$ $g^{-1}_{cat.}$ at −0.7 V (vs RHE), 97.6% and 271.3 mmol $h^{-1}$ $g^{-1}_{cat.}$ at −0.8 V (vs RHE), 95.3% and 301.9 mmol $h^{-1}$ $g^{-1}_{cat.}$at −0.9 V (vs RHE), and 97.2% and 378.8 mmol $h^{-1}$ $g^{-1}_{cat.}$ at −1.0 V (vs RHE). In contrast, the electrocatalytic performances of the other two MOPs (**Fe-TATB** and **Mn-TATB** electrodes) under identical conditions are inferior to those of **Co-TATB**. We also examined the

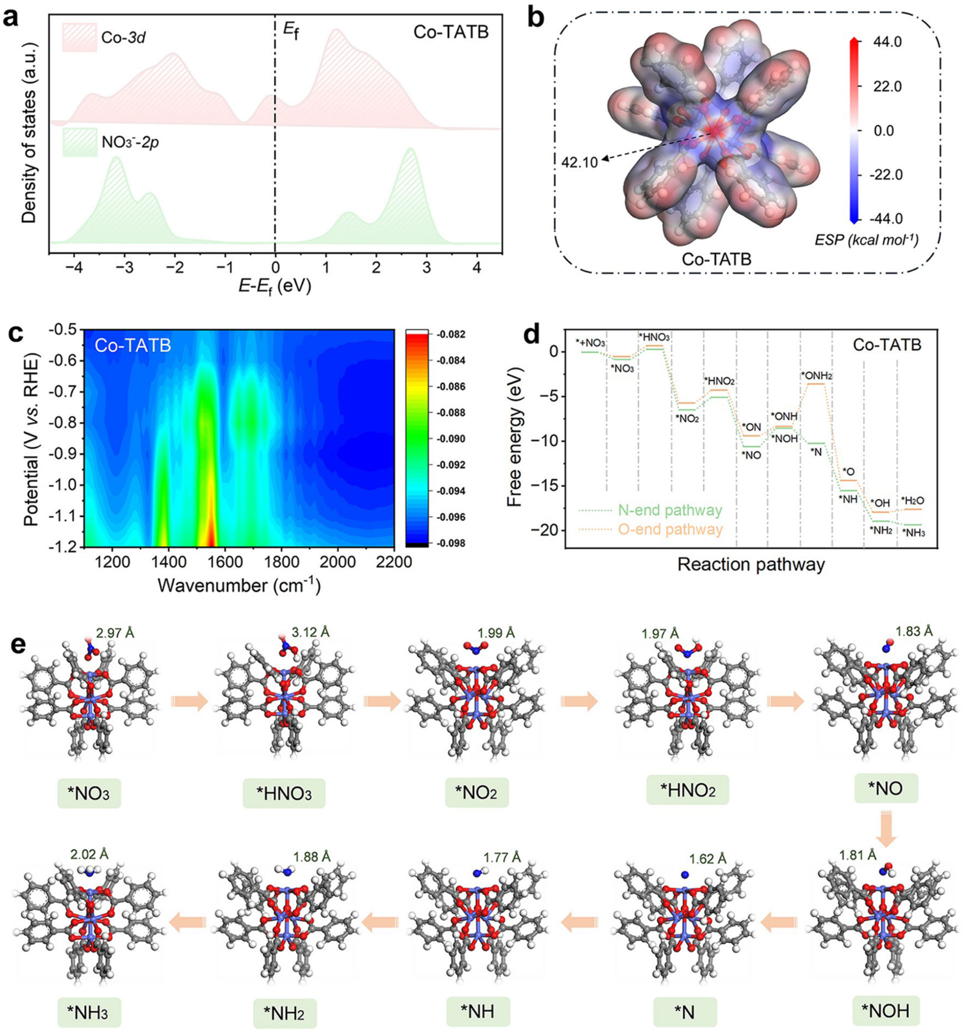

**Figure 5.** In situspectroscopic analyses and theoretical calculations. (a) Projected density of states (PDOS) analysis of Co-3*d* and $NO_3^-$-2*p* adsorbed on the **Co-TATB** model. (b) Electrostatic potential (ESP) surface of the **Co-TATB** model. (c) Contour mapping of in situ electrochemical ATR-FTIR spectra of the **Co-TATB** electrode across a range of applied potentials. (d) Calculated free energy diagrams of the potential electrocatalytic NITRR pathways on the **Co-TATB** model. (e) Optimized adsorption configurations of various reaction intermediates along the N-end pathway.

impact of varying nitrate concentrations in the electrolyte on ammonia production. With a 0.5 M $KNO_3$ electrolyte, the **Co-TATB** electrode consistently outperformed **Fe-TATB** and **Mn-TATB** electrodes, achieving an optimal $FE_{NH3}$ of 97.2% and an ammonia yield rate of 184.4 mmol $h^{-1}$ $g^{-1}{}_{cat.}$. In comparison, **Fe-TATB** and **Mn-TATB** reached optimal $FE_{NH3}$ values of 84.3 and 66.2%, respectively (Figure 4d).

Long-term stability is also a crucial factor in assessing the robustness of electrocatalysts. The electrocatalytic stability of the **Co-TATB** electrode was evaluated through cycling tests, as depicted in Figure 4e. After eight cycles, the $FE_{NH3}$ at −0.7 V (vs RHE) remained constant in the 0.1 M $Na_2SO_4$-0.1 M $KNO_3$ electrolyte, with minimal fluctuations observed in each cycle. Figure S21 displays the nitrogenous product ratios during the NITRR on the **Co-TATB** electrode at different applied potentials. In the 0.1 M $Na_2SO_4$-0.1 M $KNO_3$ electrolyte, only trace amounts of nitrite ($NO_2^-$) were detected, indicating a high selectivity for electrochemical $NO_3^-$-to-$NH_3$ conversion. The phosphate-buffered saline (PBS) buffer solution was generally used as a pH stabilizer and supporting electrolyte in electrochemical reactions. In this study, the NITRR was also evaluated in 0.1 M $KNO_3$-containing 0.1 M PBS buffer, indicating superior $NH_3$-producing activity (Figure S22). Figure S23 shows the stable $NH_3$ production performance of the Co-TATB electrode during a 300,000 s chronoamperometry test, exhibiting no obvious decline in FE toward $NH_3$ electrosynthesis. This indicates excellent durability during the long-term NITRR process. While demonstrating excellent long-term NITRR durability, the current−time curve reveals a slight upward trend from 10 h onward, suggesting a mild catalyst deactivation. $^{15}N$-labeled nitrate (98.3% enriched $Na^{15}NO_3$) was employed to trace the nitrogen source of the produced ammonia. The $^1H$ NMR analysis (Figure 4f) clearly showed distinct $^{15}NH_4^+$ doublets in the electrolyte after the NITRR, contrasting with the characteristic triplets of $^{14}NH_4^+$ when using natural abundance of nitrate. These isotopic signatures unambiguously demonstrate that the electrogenerated ammonia derives from nitrate reduction rather than from other potential nitrogen sources.

The practical viability of the designed MOP electrodes for the NITRR depends on achieving industrial-level current densities. In this study, we present a custom flow cell system for conducting NITRR tests, as illustrated in Figure 4g. The LSV curve of the **Co-TATB** electrode, measured in the flow cell with a mixed 0.1 M $Na_2SO_4$−0.1 M $KNO_3$ electrolyte, demonstrates a dramatic rise of the current density in comparison with that obtained in a pure 0.2 M KCl electrolyte across the voltage range of 0.3 to −0.6 V (vs RHE), confirming the occurrence of the NITRR process (Figure S24). To evaluate the catalytic stability during the long-term NITRR test, the time-dependent current density curve of the **Co-TATB** electrode was measured in the flow cell over a 10-h period at −0.5 V (vs RHE), yielding an average current density of 332.1 mA $cm^{-2}$, as shown in Figure 4h. Notably, there was no significant decrease in $FE_{NH3}$ during the testing duration. The $I-t$ curve indicated a slight upward trend after ∼5 h, suggesting a minor attenuation of catalytic activity. The electrocatalytic performances of **Co-TATB** and **Fe-TATB** were compared with representative electrocatalysts in previous literature (Figure 4i), revealing that they outperform many leading ammonium-producing electrocatalysts in terms of $FE_{NH3}$ values.[30−45]

Electrochemical impedance spectroscopy (EIS) measurements revealed distinct charge transfer characteristics between the MOP electrodes (Figure S25). The Nyquist plots showed that **Co-TATB** and **Fe-TATB** exhibited a significantly reduced charge transfer resistance ($R_{ct}$) compared to **Mn-TATB**, suggesting enhanced electron mobility in these electrode materials. Comparative electrochemical surface area analysis was conducted to evaluate the intrinsic catalytic properties of the **Mn-TATB**, **Fe-TATB**, and **Co-TATB** electrodes. Cyclic voltammetry measurements in the potential window of −0.35 to −0.45 V (vs Ag/AgCl) enabled the determination of double-layer capacitances through linear regression analysis of current density differences at −0.40 V versus scan rate. The calculated $C_{dl}$ values revealed that **Co-TATB** (0.21 mF $cm^{-2}$) possessed a slightly greater electrochemically active surface area than **Mn-TATB** (0.16 mF $cm^{-2}$) and **Mn-TATB** (0.15 mF $cm^{-2}$), as shown in Figure S26. This enhanced capacitance directly correlates with increased availability of active sites for nitrate reduction intermediates. To probe the active sites, we introduced a known strong coordinating agent of 0.1 M KSCN for transition metals into the nitrate-containing electrolyte (0.1 M $KNO_3$/0.1 M $Na_2SO_4$). This competitive ligand effectively blocked access to metal centers, as evidenced by the dramatic current density reduction relative to the SCN-free system (Figure S27). These results confirm that the cobalt centers in **Co-TATB** predominantly mediate the nitrate reduction reaction. Structural characterizations of the **Co-TATB** electrode were performed before and after extended nitrate reduction for 300,000 s using multiple analytical techniques. Powder X-ray diffraction analysis (Figure S28) revealed a transition to amorphous phase formation following prolonged electrocatalysis, while scanning electron microscopy and elemental mapping (Figure S29) provided complementary characterizations of morphological changes induced by the NITRR process.

**In Situ Spectroscopic Analyses and Mechanism Studies.** To gain insights into the intrinsic structure−performance relationship, density functional theory (DFT) calculations were employed to investigate the electronic structure of the square-planar tetranuclear metal center in the **Co-TATB** model. Projected density of states (PDOS) analysis of $*NO_3$ adsorption revealed strong interactions between the Co $3d$ orbitals and $NO_3^-$, with the Co $3d$ orbitals positioned near the Fermi level ($E_f$), indicating enhanced catalytic activity (Figure 5a). The significant orbital overlap between Co $3d$ and $NO_3^-$ orbitals ensures stable adsorption, facilitating the subsequent NITRR process. Electrostatic potential (ESP) analysis further demonstrates a highly positive ESP value (42.10 kcal $mol^{-1}$) at the Co sites, which favors the adsorption of nucleophilic $NO_3^-$ (Figure 5b). Charge transfer analysis confirms the transfer of 0.40 electrons from the Co atom to the $NO_3^-$ moiety, suggesting that the Co site acts as the active center for NITRR (Figure S30).

To investigate the intrinsic electrocatalytic mechanism during the NITRR process, in situ attenuated total reflectance FTIR (ATR-FTIR) spectroscopy was conducted using a three-electrode configuration with applied potentials ranging from −0.5 to −1.2 V (vs RHE), as illustrated in Figures 5c and S31. An upward absorption band observed at near 1384 $cm^{-1}$ corresponds to the N−O symmetric stretching vibration in $NO_3^-$, reflecting a continuous consumption of nitrate species.[46] Additionally, several peaks attributable to different nitrogenous intermediates appear concurrently. The peak at approximately 1278 $cm^{-1}$ relates to the N−O antisymmetric stretching vibration of $NO_2^-$.[35,47−51] The peaks at ∼1515 and ∼1647 $cm^{-1}$ correspond to the stretching modes of NO, representing the deoxygenation processes that occur during the reduction of nitrate.[35,47−49,52] Notably, the peak observed around 1459 $cm^{-1}$ is associated with the $\sigma$(N−H) bending mode for $NH_4^+$ species, verifying the hydrodeoxygenation process and ammonia production.[35,47,53−55]

The Gibbs free energy differences associated with various NITRR pathways for the **Co-TATB** model were evaluated by the DFT method, as shown in Figure 5d. The NITRR process started with the adsorption of $NO_3^-$, which was pivotal to the reaction sequence. Upon adsorption at the Co site, $NO_3^-$ was susceptible to proton attack, leading to the formation of the $*HNO_3$ intermediate. The transformation from $*HNO_3$ to $*NO_2$ occurred in an exothermic manner, demonstrating a free energy decrease of ∼−6.82 eV and releasing the first $H_2O$ molecule. Subsequently, the conversion from $*NO_2$ to $*HNO_2$ resulted in a free energy increase of ∼1.43 eV. To explore possible NITRR pathways, we further examined the NO molecules configured with N-end and O-end orientations. The optimized adsorption geometries of various reaction intermediates along these pathways are presented in Figures 5e and S32. The subsequent *ONH hydrogenation step toward the $*ONH_2$ intermediate along the O-end pathway proved to be challenging, with a significant energy requirement of ∼ 4.76 eV. Consequently, the N-end pathway was identified as more favorable for further investigation due to its lower energetic barrier compared to the O-end pathway. In the N-end pathway, the *NOH intermediate could be attacked by four $H^+/e^-$ pairs at the metal Co sites, ultimately leading to the formation of the target ammonium molecule, with these steps being exothermic. The catalytic cycle concluded with desorption of the ammonium molecule from the **Co-TATB** surface, achieving a high ammonia production rate.

## ■ CONCLUSIONS

In summary, we report the construction of a series of high-symmetry coordination MOPs with varying metal centers combined with TATB ligands, allowing us to elucidate the inherent structure−performance relationship and reaction mechanism in the electrochemical NITRR. The square-planar metal coordination structures of these MOPs enhance the number of available active sites, reduce steric hindrance, and improve both reactant and electron transfer. These structures also promote H* adsorption, in contrast with polyhedral coordination, such as tetrahedral structures, which hinder H* adsorption and create less favorable spatial configurations for subsequent catalytic reactions. Among the MOP electrodes, **Co-TATB** demonstrated the highest activity, with the trend following Co > Fe > Mn. The **Co-TATB** exhibits a remarkable $FE_{NH3}$ of ∼98% across a broad voltage range (−0.7 V to −1.0 V (vs RHE)). When operated in a flow cell at an industrially relevant current density of ∼332.1 mA $cm^{-2}$, the **Co-TATB** electrode presented excellent long-term stability. By integrating in situ spectroscopic analyses with theoretical calculations, we identified the most probable NITRR pathway for the **Co-TATB** model. Overall, this study offers meaningful insights for the rational design of next-generation electrocatalysts, leveraging highly symmetric metal−organic coordination networks to facilitate the efficient and selective conversion of small molecules into high-value products.

## ■ ASSOCIATED CONTENT

### Supporting Information

The Supporting Information is available free of charge at https://pubs.acs.org/doi/10.1021/jacs.5c06650.

Experimental methods, computational details, three-dimensional crystal structures of MOPs, PXRD, solid-state UV−vis−NIR spectra, TGA, TEM, LSV, *I*−*t* curves, CV, EIS, UV−vis absorption spectra, NITRR product selectivity diagram, in situ electrochemical ATR-FTIR spectra, charge density difference diagram of $NO_3^-$, optimized geometric structures of reaction intermediates, table of fitted results for the coordination environments of samples, Figures S1−S32, and supporting references (PDF)

## ■ AUTHOR INFORMATION

### Corresponding Authors

**Jing-Lin Zuo** − *State Key Laboratory of Coordination Chemistry, MOE Key Laboratory of Mesoscopic Chemistry, MOE Key Laboratory of High Performance Polymer Materials and Technology, Jiangsu Key Laboratory of Advanced Organic Materials, Suzhou Key Laboratory of Green Intelligent Manufacturing of New Energy Materials and Devices, Tianchang New Materials and Energy Technology Research Center, Institute of Green Chemistry and Engineering, School of Chemistry and Chemical Engineering, Nanjing University, Nanjing, Jiangsu 210023, P. R. China;* orcid.org/0000-0003-1219-8926; Email: zuojl@nju.edu.cn

**Jian Su** − *State Key Laboratory of Coordination Chemistry, MOE Key Laboratory of Mesoscopic Chemistry, MOE Key Laboratory of High Performance Polymer Materials and Technology, Jiangsu Key Laboratory of Advanced Organic Materials, Suzhou Key Laboratory of Green Intelligent Manufacturing of New Energy Materials and Devices, Tianchang New Materials and Energy Technology Research Center, Institute of Green Chemistry and Engineering, School of Chemistry and Chemical Engineering, Nanjing University, Nanjing, Jiangsu 210023, P. R. China; School of Chemistry and Chemical Engineering, Nanjing University of Science and Technology, Nanjing, Jiangsu 210094, P. R. China;* Email: sujian@njust.edu.cn

**Zhong Jin** − *State Key Laboratory of Coordination Chemistry, MOE Key Laboratory of Mesoscopic Chemistry, MOE Key Laboratory of High Performance Polymer Materials and Technology, Jiangsu Key Laboratory of Advanced Organic Materials, Suzhou Key Laboratory of Green Intelligent Manufacturing of New Energy Materials and Devices, Tianchang New Materials and Energy Technology Research Center, Institute of Green Chemistry and Engineering, School of Chemistry and Chemical Engineering, Nanjing University, Nanjing, Jiangsu 210023, P. R. China;* orcid.org/0000-0001-8860-8579; Email: zhongjin@nju.edu.cn

### Authors

**Miao Wang** − *State Key Laboratory of Coordination Chemistry, MOE Key Laboratory of Mesoscopic Chemistry, MOE Key Laboratory of High Performance Polymer Materials and Technology, Jiangsu Key Laboratory of Advanced Organic Materials, Suzhou Key Laboratory of Green Intelligent Manufacturing of New Energy Materials and Devices, Tianchang New Materials and Energy Technology Research Center, Institute of Green Chemistry and Engineering, School of Chemistry and Chemical Engineering, Nanjing University, Nanjing, Jiangsu 210023, P. R. China*

**Ya-Ru Meng** − *School of Chemistry and Chemical Engineering, Nanjing University of Science and Technology, Nanjing, Jiangsu 210094, P. R. China*

**Wenjie Xu** − *National Synchrotron Radiation Laboratory, Chinese Academy of Sciences Center for Excellence in Nanoscience, University of Science and Technology of China, Hefei, Anhui 230029, P. R. China*

**Tianyu Shen** − *State Key Laboratory of Coordination Chemistry, MOE Key Laboratory of Mesoscopic Chemistry, MOE Key Laboratory of High Performance Polymer Materials and Technology, Jiangsu Key Laboratory of Advanced Organic Materials, Suzhou Key Laboratory of Green Intelligent Manufacturing of New Energy Materials and Devices, Tianchang New Materials and Energy Technology Research Center, Institute of Green Chemistry and Engineering, School of Chemistry and Chemical Engineering, Nanjing University, Nanjing, Jiangsu 210023, P. R. China*

**Yunhao Wang** − *Department of Chemistry, Hong Kong Branch of National Precious Metals Material Engineering Research Center (NPMM), Hong Kong Institute for Clean Energy, City University of Hong Kong, Kowloon, Hong Kong 999077, P. R. China*

**Qianchuan Yu** − *State Key Laboratory of Coordination Chemistry, MOE Key Laboratory of Mesoscopic Chemistry, MOE Key Laboratory of High Performance Polymer Materials and Technology, Jiangsu Key Laboratory of Advanced Organic Materials, Suzhou Key Laboratory of Green Intelligent Manufacturing of New Energy Materials and Devices, Tianchang New Materials and Energy Technology Research Center, Institute of Green Chemistry and Engineering, School of Chemistry and Chemical Engineering, Nanjing University, Nanjing, Jiangsu 210023, P. R. China*

**Chongjing Liu** − *National Synchrotron Radiation Laboratory, Chinese Academy of Sciences Center for Excellence in*

*Nanoscience, University of Science and Technology of China, Hefei, Anhui 230029, P. R. China*

**Yuming Gu** − *State Key Laboratory of Coordination Chemistry, MOE Key Laboratory of Mesoscopic Chemistry, MOE Key Laboratory of High Performance Polymer Materials and Technology, Jiangsu Key Laboratory of Advanced Organic Materials, Suzhou Key Laboratory of Green Intelligent Manufacturing of New Energy Materials and Devices, Tianchang New Materials and Energy Technology Research Center, Institute of Green Chemistry and Engineering, School of Chemistry and Chemical Engineering, Nanjing University, Nanjing, Jiangsu 210023, P. R. China;* orcid.org/0000-0003-1366-831X

**Zuoxiu Tie** − *State Key Laboratory of Coordination Chemistry, MOE Key Laboratory of Mesoscopic Chemistry, MOE Key Laboratory of High Performance Polymer Materials and Technology, Jiangsu Key Laboratory of Advanced Organic Materials, Suzhou Key Laboratory of Green Intelligent Manufacturing of New Energy Materials and Devices, Tianchang New Materials and Energy Technology Research Center, Institute of Green Chemistry and Engineering, School of Chemistry and Chemical Engineering, Nanjing University, Nanjing, Jiangsu 210023, P. R. China*

**Zhanxi Fan** − *Department of Chemistry, Hong Kong Branch of National Precious Metals Material Engineering Research Center (NPMM), Hong Kong Institute for Clean Energy, City University of Hong Kong, Kowloon, Hong Kong 999077, P. R. China;* orcid.org/0000-0003-3133-6503

Complete contact information is available at: https://pubs.acs.org/10.1021/jacs.5c06650

### Author Contributions

$^{\perp}$M.W., Y.-R.M., W.X., and T.S. contributed equally to this work.

### Notes

The authors declare no competing financial interest.

## ACKNOWLEDGMENTS

The authors appreciate the financial support from the National Natural Science Foundation of China (22479074, 22475096, 22275084, and 22301135), the Fundamental Research Funds for the Central Universities (30922010301), the General Project of the Joint Fund of Equipment Preresearch and the Ministry of Education (8091B02052407), the Natural Science Foundation of Jiangsu Province (BK20240400, BK20241236, BK20243010 and BK20220928), the Science and Technology Major Project of Jiangsu Province (BG2024013), the Scientific and Technological Achievements Transformation Special Fund of Jiangsu Province (BA2023037), the Academic Degree and Postgraduate Education Reform Project of Jiangsu Province (JGKT24_C001), the Key Core Technology Open Competition Project of Suzhou City (SYG2024122), the open research fund of Suzhou Laboratory (SZLAB-1308-2024-TS005), the Gusu Leading Talent Program of Scientific and Technological Innovation and Entrepreneurship of Wujiang District in Suzhou City (ZXL2021273), and the Chenzhou National Sustainable Development Agenda Innovation Demonstration Zone Provincial Special Project (2023sfq11).

## REFERENCES

(1) Service, R. F. New recipe produces ammonia from air, water, and sunlight. *Science* **2014**, *345*, 610−610.

(2) Tang, C.; Qiao, S. Z. How to explore ambient electrocatalytic nitrogen reduction reliably and insightfully. *Chem. Soc. Rev.* **2019**, *48* (12), 3166−3180.

(3) Good, A. Toward nitrogen-fixing plants. *Science* **2018**, *359*, 869−870.

(4) Shi, R.; Zhang, X.; Waterhouse, G.; Zhao, X.; Zhang, R. The journey toward low temperature, low pressure catalytic nitrogen fixation. *Adv. Energy Mater.* **2020**, *10*, No. 2000659.

(5) Zhang, J.; Tian, X.; Liu, M.; Guo, H.; Zhou, J.; Fang, Q.; Liu, Z.; Wu, Q.; Lou, J. Cobalt-modulated molybdenum−dinitrogen interaction in $MoS_2$ for catalyzing ammonia synthesis. *J. Am. Chem. Soc.* **2019**, *141*, 19269−19275.

(6) Hui, L.; Xue, Y.; Yu, H.; Liu, Y.; Fang, Y.; Xing, C.; Huang, B.; Li, Y. Highly efficient and selective generation of ammonia and hydrogen on a graphdiyne-based catalyst. *J. Am. Chem. Soc.* **2019**, *141*, 10677−10683.

(7) Zhang, L.; Ding, L.; Chen, G.; Yang, X.; Wang, H. Ammonia synthesis under ambient conditions: Selective electroreduction of dinitrogen to ammonia on black phosphorus nanosheets. *Angew. Chem., Int. Ed.* **2019**, *131*, 2638−2642.

(8) Li, S.; Bao, D.; Shi, M.; Wulan, B.; Yan, J.; Jiang, Q. Amorphizing of Au nanoparticles by $CeO_x$-RGO hybrid support towards highly efficient electrocatalyst for $N_2$ reduction under ambient conditions. *Adv. Mater.* **2017**, *29*, No. 1700001.

(9) Yu, B.; Li, H.; White, J.; Donne, S.; Yi, J.; Xi, S.; Fu, Y.; Henkelman, G.; Yu, H.; Chen, Z.; Ma, T. Tuning the catalytic preference of ruthenium catalysts for nitrogen reduction by atomic dispersion. *Adv. Funct. Mater.* **2020**, *30*, No. 1905665.

(10) Jiang, M.; Han, L.; Peng, P.; Hu, Y.; Xiong, Y.; Mi, C.; Tie, Z.; Xiang, Z.; Jin, Z. Quasi-phthalocyanine conjugated covalent organic frameworks with nitrogen-coordinated transition metal centers for high-efficiency electrocatalytic ammonia synthesis. *Nano Lett.* **2022**, *22* (1), 372−379.

(11) Gao, Q.; Pillai, H. S.; Huang, Y.; Liu, S.; Mu, Q.; Han, X.; Yan, Z.; Zhou, H.; He, Q.; Xin, H.; Zhu, H. Breaking adsorption-energy scaling limitations of electrocatalytic nitrate reduction on intermetallic CuPd nanocubes by machine-learned insights. *Nat. Commun.* **2022**, *13* (1), 2338.

(12) Liu, C.; Zhang, G.; Zhang, W.; Gu, Z.; Zhu, G. Specifically adsorbed ferrous ions modulate interfacial affinity for high-rate ammonia electrosynthesis from nitrate in neutral media. *Proc. Natl. Acad. Sci. U. S. A.* **2023**, *120*, No. e2209979120.

(13) Zhang, X.; Wang, Y.; Liu, C.; Yu, Y.; Lu, S.; Zhang, B. Recent advances in non-noble metal electrocatalysts for nitrate reduction. *Chemical Engineering Journal* **2021**, *403*, No. 126269.

(14) Langevelde, P. H.; Katsounaros, I.; Koper, M. T. M. Electrocatalytic nitrate reduction for sustainable ammonia production. *Joule* **2021**, *5*, 290−294.

(15) Wang, Z.; Young, S. D.; Goldsmith, B. R.; Singh, N. Increasing electrocatalytic nitrate reduction activity by controlling adsorption through PtRu alloying. *J. Catal.* **2021**, *395*, 143−154.

(16) Zhang, R.; Hong, H.; Liu, X.; Zhang, S.; Li, C.; Cui, H.; Wang, Y.; Liu, J.; Hou, Y.; Li, P.; Huang, Z.; Guo, Y.; Zhi, C. Molecular engineering of a metal-organic polymer for enhanced electrochemical nitrate-to-ammonia conversion and zinc nitrate batteries. *Angew. Chem., Int. Ed.* **2023**, *62*, No. e202309930.

(17) Zheng, S.; Dong, X.; Chen, H.; Huang, R.; Cai, J.; Zang, S. Unveiling ionized interfacial water-induced localized H* enrichment for electrocatalytic nitrate reduction. *Angew. Chem., Int. Ed.* **2024**, *64*, No. e202413033.

(18) Xie, L. S. Electrically conductive metal-organic frameworks. *Chem. Rev.* **2020**, *120* (16), 8536−8580.

(19) Yang, Q.; Xu, Q.; Jiang, H.-L. Metal-organic frameworks meet metal nanoparticles: synergistic effect for enhanced catalysis. *Chem. Soc. Rev.* **2017**, *46* (15), 4774−4808.

(20) Jiao, L.; Wang, Y.; Jiang, H.-L.; Xu, Q. Metal-organic frameworks as platforms for catalytic applications. *Adv. Mater.* **2018**, *30* (37), No. 1703663.

(21) Xiong, Y.; Li, B.; Gu, Y.; Yan, T.; Ni, Z.; Li, S.; Zuo, J.; Ma, J.; Jin, Z. Photocatalytic nitrogen fixation under an ambient atmosphere using a porous coordination polymer with bridging dinitrogen anions. *Nat. Chem.* **2023**, *15* (2), 286−293.

(22) Jiang, Z.; Wang, Y.; Lin, Z.; Yuan, Y.; Zhang, X.; Tang, Y.; Wang, H.; Li, H.; Jin, C.; Liang, Y. Molecular electrocatalysts for rapid and selective reduction of nitrogenous waste to ammonia. *Energy Environ. Sci.* **2023**, *16* (5), 2239−2246.

(23) Ma, S.; Zhou, H.-C. A metal-organic framework with entatic metal centers exhibiting high gas adsorption affinity. *J. Am. Chem. Soc.* **2006**, *128*, 11734−11735.

(24) Su, J.; Yuan, S.; Wang, H.-Y.; Huang, L.; Ge, J.-Y.; Joseph, E.; Qin, J.; Cagin, T.; Zuo, J.-L.; Zhou, H.-C. Redox-switchable breathing behavior in tetrathiafulvalene-based metal−organic frameworks. *Nat. Commun.* **2017**, *8* (1), 2008.

(25) Zhang, Z.; Lv, Y.; Gu, Y.; Zhou, X.; Tian, B.; Zhang, A.; Yang, Z.; Chen, S.; Ma, J.; Ding, M.; Zuo, J.-L. Dual $Zn_5$-$NiS_4$ sites in a redox-active metal-organic framework enables efficient cascade catalysis for nitrate-to-ammonia conversion. *Angew. Chem., Int. Ed.* **2024**, *64*, No. e202418272.

(26) Sun, L.; Reddu, V.; Xi, S.; Dai, C.; Sheng, Y.; Su, T.; Fisher, A. C.; Wang, X. Cobalt quaterpyridine complexes for highly efficient heterogeneous $CO_2$ reduction in aqueous media. *Adv. Energy Mater.* **2022**, *12* (34), No. 2202108.

(27) Wang, M.; Li, S.; Gu, Y.; Xu, W.; Wang, H.; Sun, J.; Chen, S.; Tie, Z.; Zuo, J.; Ma, J.; Su, J.; Jin, Z. Polynuclear cobalt cluster-based coordination polymers for efficient nitrate-to-ammonia electroreduction. *J. Am. Chem. Soc.* **2024**, *146*, 20439−20448.

(28) Haandel, L.; Smolentsev, G.; Bokhoven, J.; Hensen, E.; Weber, T. Evidence of octahedral Co-Mo-S sites in hydrodesulfurization catalysts as determined by resonant inelastic X-ray scattering and X-ray absorption spectroscopy. *ACS Catal.* **2020**, *10* (19), 10978−10988.

(29) Tang, P.; Gao, P.; Cui, X.; Chen, Z.; Fu, Q.; Wang, Z.; Mo, Y.; Liu, H.; Xu, C.; Liu, J.; Yan, J.; Passerini, S. Covalency competition induced active octahedral sites in spinel cobaltites for enhanced pseudocapacitive charge storage. *Adv. Energy Mater.* **2022**, *12* (2), No. 2102053.

(30) Liu, L.; Xiao, T.; Fu, H.; Chen, Z.; Qu, X.; Zheng, S. Construction and identification of highly active single-atom Fe1-NC catalytic site for electrocatalytic nitrate reduction. *Applied Catalysis B: Environmental* **2023**, *323*, No. 122181.

(31) Dai, X.; Tian, L.; Liu, Z.; Xu, W.; Liu, Y.; Liu, Y. Nanoreactor based on cyclodextrin for direct electrocatalyzed ammonia synthesis. *ACS Nano* **2022**, *16* (11), 18398−18407.

(32) Wang, J.; Cai, C.; Wang, Y.; Yang, X.; Wu, D.; Zhu, Y.; Li, M.; Gu, M.; Shao, M. Electrocatalytic reduction of nitrate to ammonia on low-cost ultrathin $CoO_x$ nanosheets. *ACS Catal.* **2021**, *11* (24), 15135−15140.

(33) Xie, M.; Tang, S.; Li, Z.; Wang, M.; Jin, Z.; Li, P.; Zhan, X.; Zhou, H.; Yu, G. Intermetallic single-atom alloy In-Pd bimetallene for neutral electrosynthesis of ammonia from nitrate. *J. Am. Chem. Soc.* **2023**, *145* (25), 13957−13967.

(34) Yu, Y.; Wang, C.; Yu, Y.; Wan, Y.; Zhang, B. Promoting selective electroreduction of nitrates to ammonia over electron-deficient co modulated by rectifying schottky contacts. *Sci. China Chem.* **2020**, *63*, 1469−1476.

(35) Zhang, N.; Shang, J.; Deng, X.; Cai, L.; Long, R.; Xiong, Y.; Chai, Y. Governing interlayer strain in bismuth nanocrystals for efficient ammonia electrosynthesis from nitrate reduction. *ACS Nano* **2022**, *16* (3), 4795−4804.

(36) Li, L.; Tang, C.; Cui, X.; Zheng, Y.; Wang, X.; Xu, H.; Zhang, S.; Shao, T.; Davey, K.; Qiao, S. Efficient nitrogen fixation to ammonia through integration of plasma oxidation with electrocatalytic reduction. *Angew. Chem., Int. Ed.* **2021**, *133* (25), 14250−14256.

(37) Lv, Y.; Ke, S.-W.; Gu, Y.; Tian, B.; Tang, L.; Ran, P.; Zhao, Y.; Ma, J.; Zuo, J.-L.; Ding, M. Highly efficient electrochemical nitrate reduction to ammonia in strong acid conditions with $Fe_2M$-trinuclear-cluster metal-organic frameworks. *Angew. Chem., Int. Ed.* **2023**, *62* (27), No. e202305246.

(38) Jiang, M.; Zhu, Q.; Song, X.; Gu, Y.; Zhang, P.; Li, C.; Cui, J.; Ma, J.; Tie, Z.; Jin, Z. Batch-Scale Synthesis of nanoparticle-agminated 3D porous $Cu@Cu_2O$ microspheres for highly-selective electrocatalysis of nitrate to ammonia. *Environ. Sci. Technol.* **2022**, *56* (14), 10299−10307.

(39) Hu, H.; Miao, R.; Yang, F.; Duan, F.; Zhu, H.; Hu, Y.; Du, M.; Lu, S. Intrinsic activity of metalized porphyrin-based covalent organic frameworks for electrocatalytic nitrate reduction. *Adv. Energy Mater.* **2024**, *14* (6), No. 2302608.

(40) Chen, G.; Yuan, Y.; Jiang, H.; Ren, S.; Ding, L.; Ma, L.; Wu, T.; Lu, J.; Wang, H. Electrochemical reduction of nitrate to ammonia via direct eight-electron transfer using a copper-molecular solid catalyst. *Nature Energy* **2020**, *5* (8), 605−613.

(41) Chaplin, B. P.; Shapley, J. R.; Werth, C. J. The selectivity and sustainability of a Pd-In/-$Al_2O_3$ catalyst in a packed-bed reactor: the effect of solution composition. *Catal. Lett.* **2009**, *130*, 56−62.

(42) Wu, Z.-Y.; Karamad, M.; Yong, X.; Huang, Q.; Cullen, D. A.; Zhu, P.; Xia, C.; Xiao, Q.; Shakouri, M.; Chen, F.-Y.; Kim, J. Y.; Xia, Y.; Heck, K.; Hu, Y.; Wong, M. S.; Li, Q.; Gates, I.; Siahrostami, S.; Wang, H. Electrochemical ammonia synthesis via nitrate reduction on Fe single atom catalyst. *Nat. Commun.* **2021**, *12* (1), 2870.

(43) Gao, Z.; Lai, Y.; Tao, Y.; Xiao, L.; Zhang, L.; Luo, F. Constructing well-defined and robust Th-MOF-supported single-site copper for production and storage of ammonia from electroreduction of nitrate. *ACS Central Science* **2021**, *7* (6), 1066−1072.

(44) Wang, Y.; Zhou, W.; Jia, R.; Yu, Y.; Zhang, B. Unveiling the activity origin of a copper-based electrocatalyst for selective nitrate reduction to ammonia. *Angew. Chem., Int. Ed.* **2020**, *59* (13), 5350−5354.

(45) Jia, R.; Wang, Y.; Wang, C.; Ling, Y.; Yu, Y.; Zhang, B. Boosting selective nitrate electroreduction to ammonium by constructing oxygen vacancies in $TiO_2$. *ACS Catal.* **2020**, *10* (6), 3533−3540.

(46) Fang, J.; Zheng, Q.-Z.; Lou, Y.-Y.; Zhao, K.-M.; Hu, S.-N.; Li, G.; Akdim, O.; Huang, X.-Y.; Sun, S.-G. Ampere-level current density ammonia electrochemical synthesis using CuCo nanosheets simulating nitrite reductase bifunctional nature. *Nat. Commun.* **2022**, *13* (1), 7899.

(47) Song, Z.; Liu, Y.; Zhong, Y.; Guo, Q.; Zeng, J.; Geng, Z. Efficient electroreduction of nitrate into ammonia at ultralow concentrations via an enrichment effect. *Adv. Mater.* **2022**, *34* (36), No. e2204306.

(48) Bae, S.-E.; Stewart, K. L.; Gewirth, A. A. Nitrate adsorption and reduction on Cu(100) in acidic solution. *J. Am. Chem. Soc.* **2007**, *129* (33), 10171−10180.

(49) Figueiredo, M. C.; Solla-Gullón, J.; Vidal-Iglesias, F. J.; Climent, V.; Feliu, J. M. Nitrate reduction at Pt(100) single crystals and preferentially oriented nanoparticles in neutral media. *Catal. Today* **2013**, *202*, 2−11.

(50) Hao, R.; Tian, L.; Wang, C.; Wang, L.; Liu, Y.; Wang, G.; Li, W.; Ozin, G. A. Pollution to solution: A universal electrocatalyst for reduction of all $NO_x$-based species to $NH_3$. *Chem. Catalysis* **2022**, *2* (3), 622−638.

(51) Figueiredo, M. C.; Souza-Garcia, J.; Climent, V.; Feliu, J. M. Nitrate reduction on Pt(111) surfaces modified by Bi adatoms. *Electrochem. Commun.* **2009**, *11* (9), 1760−1763.

(52) Chen, L.; Li, J.; Ge, M. DRIFT study on cerium-tungsten/titania catalyst for selective catalytic reduction of $NO_x$ with $NH_3$. *Environ. Sci. Technol.* **2010**, *44* (24), 9590−9596.

(53) Pérez-Gallent, E.; Figueiredo, M. C.; Katsounaros, I.; Koper, M. T. M. Electrocatalytic reduction of Nitrate on Copper single crystals in acidic and alkaline solutions. *Electrochim. Acta* **2017**, *227*, 77−84.

(54) Zhang, N.; Jalil, A.; Wu, D.; Chen, S.; Liu, Y.; Gao, C.; Ye, W.; Qi, Z.; Ju, H.; Wang, C.; Wu, X.; Song, L.; Zhu, J.; Xiong, Y. Refining defect states in $W_{18}O_{49}$ by Mo doping: a strategy for tuning $N_2$

activation towards solar-driven nitrogen fixation. *J. Am. Chem. Soc.* **2018**, *140* (30), 9434−9443.

(55) Zhang, Y.; Zheng, H.; Zhou, K.; Ye, J.; Chu, K.; Zhou, Z.; Zhang, L.; Liu, T. Conjugated coordination polymer as a new platform for efficient and selective electroreduction of nitrate into ammonia. *Adv. Mater.* **2023**, *35* (10), No. 2209855.